PNAS RESEARCH ARTICLE | APPLIED PHYSICAL SCIENCES

Tunable nonlinear optical mapping in a multiple-scattering cavity

Yaniv Eliezer[a], Ulrich Rührmair[b,c], Nils Wisiol[d], Stefan Bittner[e,f], and Hui Cao[a,1]

Contributed by Hui Cao; received March 28, 2023; accepted June 18, 2023; reviewed by Girish Agarwal and Tsampikos Kottos

Nonlinear disordered systems are not only a model system for fundamental studies but also in high demand for practical applications. However, optical nonlinearity based on intrinsic material response is weak in random scattering systems. Here, we propose and experimentally realize a highly nonlinear mapping between the scattering potential and the emerging light of a reconfigurable multiple-scattering cavity. A quantitative analysis of the degree of nonlinearity reveals its dependence on the number of scattering events. The effective order of nonlinear mapping can be tuned over a wide range at low optical lower. The strong nonlinear mapping enhances output intensity fluctuations and long-range correlations. The flexibility, robustness, and energy efficiency of our approach provides a versatile platform for exploring such nonlinear mappings for various applications.

optical scattering | nonlinear mappings | light statistics

Significance

Nonlinear optics has a wide range of applications but requires high optical power. We propose and demonstrate an unconventional type of nonlinear mapping of a linear random-scattering cavity, based on nonlinear relation between optical scattering potential and multiply-scattered light. It is realized by reconfiguring the optical scattering potential. High-order nonlinear mapping is obtained experimentally at low optical power. The order of nonlinear mapping can be tuned over a wide range, in sharp contrast to conventional optical nonlinearity based on intrinsic material response. Our method of achieving nonlinear mapping is robust and free of temporal instability. Such nonlinear mapping also enables tuning of scattered light statistics. This work has broad applications in metrology, cryptography, artificial neural networks, and optical computing.

Structural disorder and light scattering have recently been widely explored for photonic applications (1). In most cases, the mapping between input to output fields is linear. However, nonlinear mapping is desired for various applications such as physical unclonable functions (PUFs) (2), implementation of optical neural networks, neuromorphic computing, and reservoir computing (3–7). Nonlinear mappings can be realized using nonlinear optical materials, which provide a nonlinear relation between input and output fields (8, 9). Optical nonlinearity requires high light intensity, which is hard to achieve in random media due to spatial and temporal spreading of light by scattering. While Anderson localization of light can enhance light–matter interactions, it is hard to achieve in three-dimensional disordered systems. Only low-order nonlinear processes such as second-harmonic generation have been realized in random scattering media (10–15). Furthermore, temporal instability can be induced by a quadratic electro-optical process (Kerr effect) in a disordered system (16–19).

Instead of the nonlinear relation between input and output fields, we investigate the nonlinear mapping between a reconfigurable disordered potential and emerging light of a multiple-scattering cavity. We point out that the multiple-scattering-induced nonlinear mapping is fundamentally different from the conventional nonlinear optics based on intrinsic material response. At low optical power where the intrinsic nonlinear material response is negligible, light scattering is a linear process: The output field E_o depends linearly on the input field E_i. The multiple scattering can be described by the Born series (20):

$$E_o = \mathbf{T}E_i = \left(\mathbf{V} + \mathbf{V}\mathbf{G_0}\mathbf{V} + \mathbf{V}\left[\mathbf{G_0}\mathbf{V}\right]^2 + \mathbf{V}\left[\mathbf{G_0}\mathbf{V}\right]^3 \ldots\right) E_i,$$

where $\mathbf{T}$ is a matrix that captures the linear mapping from E_i to E_o, $\mathbf{V}$ represents the scattering potential and $\mathbf{G_0}$ is the free-space Green's matrix. The first term in the expansion of $\mathbf{T}$ denotes single scattering (light scattered once), the second term double scattering, etc. In the presence of multiple scattering, the relation between the scattering potential configuration $\mathbf{V}$ and the output field E_o is nonlinear. The degree of nonlinearity increases with the number of scattering events (number of terms in $\mathbf{T}$ expansion). If single scattering dominates, the mapping from $\mathbf{V}$ to E_o is approximately linear.

Such a scheme is efficient in providing high-order nonlinear mapping at low power and also avoids temporal instability that occurs in conventional nonlinear optical systems. However, the nonlinear mapping requires reconfiguring the scattering potential. Previous studies show that the refractive-index change induced by photorefractive effect is small (21, 22), and the change by thermo-optical effect is slow (23, 24). Dynamic coupling between multiple scattered light and colloidal particles can only statistically control the motion of colloidal particles (25, 26). In the microwave regime, disordered

Author contributions: H.C. initiated the research; Y.E., U.R., and H.C. designed research; Y.E. performed research; N.W. and S.B. contributed new reagents/analytic tools; Y.E. and N.W. analyzed data; U.R. and H.C. secured funding; and Y.E. and H.C. wrote the paper.

Reviewers: G.A., Texas A&M University; and T.K., Wesleyan University College Department of Physics.

The authors declare no competing interest.

Copyright © 2023 the Author(s). Published by PNAS. This article is distributed under Creative Commons Attribution-NonCommercial-NoDerivatives License 4.0 (CC BY-NC-ND).

[1]To whom correspondence may be addressed. Email: hui.cao@yale.edu.

This article contains supporting information online at https://www.pnas.org/lookup/suppl/doi:10.1073/pnas.2305027120/-/DCSupplemental.

Published July 25, 2023.

Downloaded from https://www.pnas.org by YALE UNIVERSITY CTR FOR SCI & SOCIAL SCI INFO on July 31, 2023 from IP address 130.132.173.101.

cavities with active reconfigurable boundaries are explored for spatio-temporal focusing and power enhancement (27, 28), motion detection (29), analog computing (30), and communication (31–33). So far, the tunablity of multiple-scattering-induced nonlinear mapping has not been realized.

In this work, we create an optical scattering cavity with a reconfigurable boundary, and present a quantitative analysis of the nonlinear mapping between the scattering potential and the emerging light. High-order nonlinear mapping is obtained experimentally at low power. The effective nonlinear order can be tuned over a wide range by varying the cavity parameters. As a result of the strong nonlinear mapping, fluctuations of local and total output light intensity are enhanced, and long-range spatial correlations are established (34, 35). The greatly enhanced fluctuations facilitate light focusing and control of total transmission by optimizing the scattering potential (36). The tunable, stable, and efficient nonlinear mapping opens the door to a broad range of applications including strong optical PUFs and nonlinear optical neural networks.

1. Reconfigurable Scattering Cavity

As shown in Fig. 1*A*, our experimental setup is composed of a commercial integrating sphere (diameter 3.75 cm). Its inner surface is covered with a diffuse white reflective coating, which provides a static scattering potential. There are three openings in the sphere's boundary. The first one (diameter 8 mm) is covered by a switchable digital mirrors device (DMD), which acts as a reconfigurable scattering potential. The DMD (Texas Instruments DLP9000X) consists of 2,560 × 1,600 micromirrors, each of lateral dimension 7.6 μm can be flipped to either +15° or −15°. A continuous-wave, linearly polarized laser (Agilent 81940A) at wavelength $\lambda = 1{,}550$ nm is coupled to a single-mode fiber, which is inserted to the second opening of the integrating sphere. Input light is scattered multiple times inside the integrating sphere by the rough wall and the switchable micromirrors. The third opening (diameter 3 mm) outputs light, which is directed by a mirror to an InGaAs camera (Xenics Xeva FPA-640). A linear polarizer is placed in front of the camera, which records the speckle intensity pattern for a specific DMD configuration.

At low input power (21 mW), the output field depends linearly on the input field, in spite of multiple scattering in the integrating sphere. However, the relation between the DMD configuration and the output speckle pattern is nonlinear, because light is scattered multiple times by the DMD. We divide the micromirror array into $M_p \times M_p$ macropixels. Each macropixel has only two states $+1$ and -1, in which all constituent micromirrors are tilted by $+15°$ and $-15°$, respectively. The DMD macropixels configuration can be described by a Boolean vector X of length $M = M_p^2$ (total number of macropixels). There are 2^M possible configurations and each outputs a speckle pattern. The recorded two-dimensional intensity pattern is rearranged to a one-dimensional vector Y. Its length N is given by the number of camera pixels (100×100) within the region of interest (including ∼400 speckle grains). The exact nonlinear mapping from the k-th DMD configuration $X^{(k)}$ to the corresponding output pattern $Y^{(k)}$ is obtained with Boolean function analysis (37–40):

$$y_r^{(k)} = f\left(x_1^{(k)}, \ldots, x_M^{(k)}\right) \tag{1}$$
$$= c_0^{(n,k)} + \sum_{m_1=1}^{M} c_{m_1}^{(n,k)} x_{m_1}^{(k)} + \sum_{m_1=1}^{M} \sum_{m_2=1}^{m_1} c_{m_1,m_2}^{(n,k)} x_{m_1}^{(k)} x_{m_2}^{(k)} + \ldots + c_{1,2,\ldots,M}^{(n,k)} x_1^{(k)} x_2^{(k)} \ldots x_M^{(k)},$$

where $x_m^{(k)}$ is the m-th element of $X^{(k)}$, $y_r^{(k)}$ is the r-th element of $Y^{(k)}$, and $c_{\{\cdot\}}^{(n,k)}$ is the expansion coefficient, which is obtained by projection. See *SI Appendix*, section 1 for complete derivation.

The number of $x_m^{(k)}$ factors in each term on the right-hand-side of Eq. **1** gives the order d of that term. $d = 1$ is the linear term, and $d \geq 2$ are nonlinear terms. Larger d represents higher-order nonlinear mapping, and the maximal order is $d = M$. We obtain the expansion coefficients in Eq. **1** by fitting the measured output intensity patterns (subtracted by their average over k) for all possible DMD macropixel configurations. See *SI Appendix*, section 1 for more details. Averaging $|c_{m_1,m_2,\ldots m_d}^{(n,k)}|$ for a certain order d, over r and k, gives the mean expansion coefficient $\bar{c}(d)$ for this order. It is then normalized such that $\sum_d \bar{c}(d) = 1$. The effective order of nonlinearity is given by $\bar{d} \equiv \sum_d d\, \bar{c}(d)$.

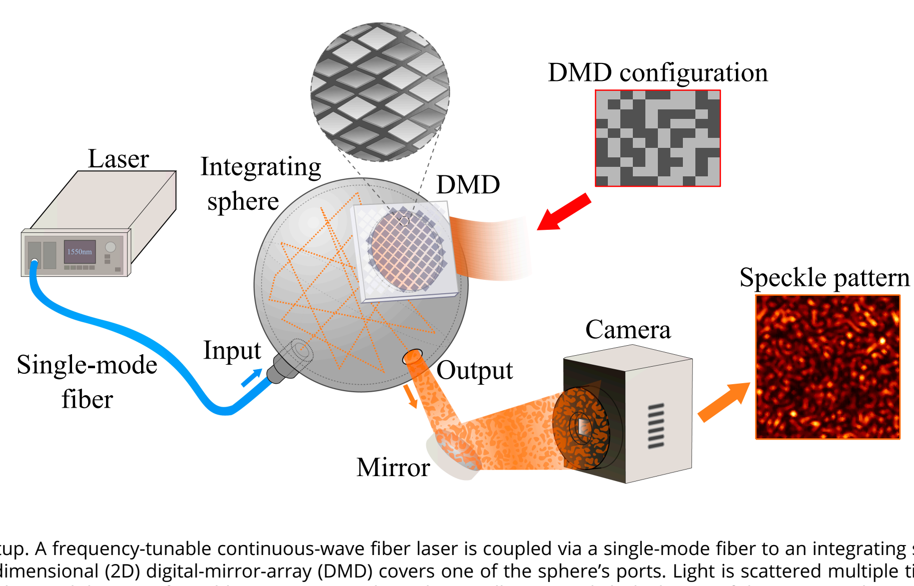

Fig. 1. Experimental setup. A frequency-tunable continuous-wave fiber laser is coupled via a single-mode fiber to an integrating sphere with an inner static rough boundary. A two-dimensional (2D) digital-mirror-array (DMD) covers one of the sphere's ports. Light is scattered multiple times inside the integrating sphere by its static boundary and the reconfigurable mirror array. Through a small opening, light leaks out of the cavity, and its intensity pattern is recorded by a digital camera.

Downloaded from https://www.pnas.org by YALE UNIVERSITY CTR FOR SCI & SOCIAL SCI INFO on July 31, 2023 from IP address 130.132.173.101.

Downloaded from https://www.pnas.org by YALE UNIVERSITY CTR FOR SCI & SOCIAL SCI INFO on July 31, 2023 from IP address 130.132.173.101.

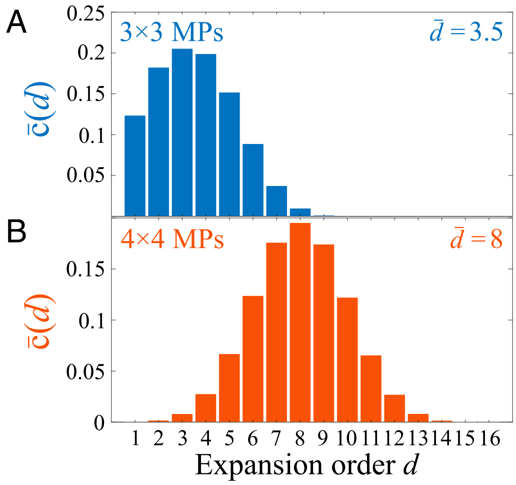

Fig. 2. Expansion coefficient $\bar{c}$ vs. order d for output light intensity with 3×3 DMD macropixels in (*A*) and 4×4 in (*B*). Note that the upper limit for d is 9 in (*A*) and 16 in (*B*). The distribution of $\bar{c}(d)$ shifts to higher order d with larger number of macropixels. The effective order of nonlinearity $\bar{d}$ increases from 3.5 (*A*) to 8.0 (*B*).

Fig. 2*A* shows the distribution of $\bar{c}(d)$ for 3×3 macropixels (2^9 configurations). $\bar{c}(d)$ spreads from $d = 1$ to $d = 8$, reaching the maximum at $d = 3$. When the number of macropixels is increased to 4×4 (Fig. 2*B*), the distribution of $\bar{c}(d)$ moves to larger d, with the maximum at $d = 8$. The mean order $\bar{d}$ increases from 3.5 to 8.0, reflecting stronger nonlinear mapping. Experimentally the total area of the DMD is fixed, and the number of macropixels determines the degree of control of the scattering potential. Hence, the effective order of nonlinear mapping increases with the degree of control of the scattering potential. We further enhance the nonlinear mapping by using 10×10 macropixels. There are 2^{100} possible configurations, which are impossible to measure and analyze to find the mean expansion order. Another way of tuning the nonlinear order is to vary the area of each macropixel, while fixing the total number of macropixels. The resulting larger area will increase the chance of scattering light, thus enhancing the nonlinear mapping.

2. Strength of Nonlinear Mapping

We expect the strength of nonlinear mapping to depend on the number of times that light scatters off the DMD. Experimentally, it is difficult to tune the number of scattering events, and we resort to numerical simulation. To save computation time, we consider a small two-dimensional (2D) cavity with a rough boundary (Fig. 3*A*). The boundary roughness is on the order of $\lambda/10$, leading to diffuse reflection of light. One side of the cavity is composed of $M = 12$ micromirrors. Each mirror (with 100% specular reflectivity) can be tilted by $+15°$ (state of $+1$) or $-15°$ (state of -1). Monochromatic light is injected through a small input port and scatters off the rough boundary and micromirrors. To vary the number of scattering events at the switchable micromirrors, we adjust light absorption by the rough boundary (away from the mirrors), so that the diffuse reflectivity ρ changes from 51% to 100%. See *SI Appendix*, section 1 for additional values of reflectivity. Part of the light leaks out of an output port, and the spatial distributions of both field and intensity are computed in a full-wave simulation of light propagation inside the cavity for each possible configuration of the $M = 12$ switchable mirrors (2^{12} in total). See *SI Appendix*, section 2 for more details on the numerical simulation. Output field and intensity patterns are stored in two matrices $\mathbf{Y_E}$ and $\mathbf{Y_I}$ correspondingly. We map the mirror configurations matrix $\mathbf{X}$ to $\mathbf{Y_E}$ and $\mathbf{Y_I}$ using Eq. **1**, for different values of boundary reflectivity ρ.

Fig. 3 *B* and *C* shows the distribution of $\bar{c}_E(d)$ for output field and that of $\bar{c}(d)$ for intensity. Both distributions shift to larger d with increasing ρ. At low boundary reflectivity, light absorption by the rough boundary reduces the number of bounces off the micromirror array. At $\rho = 51\%$, $\bar{c}_E(d)$ is peaked at $d = 1$, thus the nonlinear mapping of output field is weak (Fig. 3*B*). Correspondingly, $\bar{c}(d)$ is peaked at $d = 2$, indicating the nonlinear mapping of intensity is mostly from the square of field amplitude (Fig. 3*C*). With increasing ρ, the effective order of nonlinear mapping for both field $\bar{d}_E$ and intensity $\bar{d}$ rises monotonously, despite $\bar{d}_E$ is slightly lower than $\bar{d}$ (Fig. 3*D*). As the boundary reflectivity is higher, light has more chance of scattering off the switchable mirrors, leading to higher expansion order.

To quantify the number of bounces off the micro-mirror array, we conduct a classical ray tracing simulation in the same cavity with varying boundary reflectivity. See *SI Appendix*, section 3 for more details. Briefly, we launch many optical rays into the cavity and trace individual ray propagation until it dies out. The number of bounces off the mirrors is weighted by the intensity of the ray at each bounce to give the effective number of bounces for a single ray. Then, we average this number over all rays escaping through the output port, to obtain the mean number of bounces $\bar{\nu}$ for different ρ. Fig. 3*E* shows that $\bar{d}$ scales linearly with $\bar{\nu}$, indicating that the average number of light bounces is closely related to the expansion order.

3. Output Intensity Statistics

Next, we investigate how the nonlinear mapping influences intensity statistics of output light. Previously, "hot spots" of field intensities akin to rogue wave formation have been observed in random-scattering microwave and chaotic nanophotonic cavities (41, 42). Here, we show that highly nonlinear mapping leads to exceptional light statistics.

We observe extraordinary fluctuation of local intensity with varying scattering potential. Fig. 4*A* shows the probability density function (PDF) of output intensity normalized by its mean over all mirror configurations, $\eta_k(r) \equiv I_k(r)/\langle I_k(r)\rangle_k$, where $I_k(r)$ is light intensity at a spatial location r for the switchable-mirror configuration k. As ρ increases from 51% to 100%, the PDF $P(\eta)$ develops a heavy tail at large η, reflecting super-Rayleigh intensity statistics.

This behavior is surprising, as individual output patterns exhibit Rayleigh statistics. As seen in Fig. 4*A*, with $I_k(r)$ normalized by the spatial-average $\langle I_k(r)\rangle_r$ for individual mirror configuration: $\tilde{\eta}_k(r) \equiv I_k(r)/\langle I_k(r)\rangle_r$, the PDF $P(\tilde{\eta})$ displays an exponential decay regardless of ρ. See *SI Appendix*, section 2 for additional details. Fig. 4*C* shows that the contrast of $\tilde{\eta}$ (SD divided by mean) stays close to 1, while the contrast of η increases with the mean expansion order $\bar{d}$.

The super-Rayleigh statistics of η at high $\bar{d}$ originates from enhanced fluctuation of total output intensity with mirror configuration. Fig. 4*B* shows the PDF of normalized total intensity, $\zeta_k \equiv \int I_k(r)\,dr / \langle \int I_k(r)\,dr\rangle_k = \langle I_k(r)\rangle_r / \langle I_k(r)\rangle_{r,k}$. With increasing ρ, $P(\zeta)$ is broadened and skewed. Fig. 4*D* shows

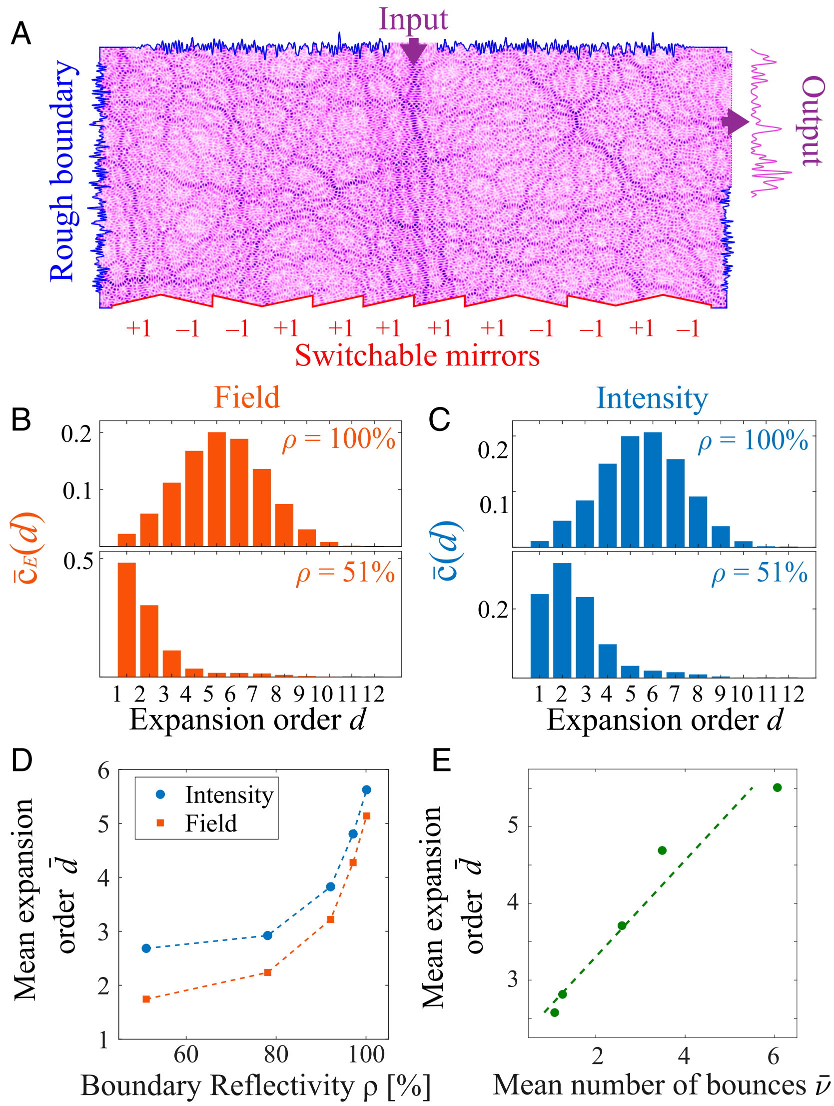

Fig. 3. Tuning of nonlinear mapping. (*A*) Steady-state solution of light distribution inside a 2D cavity (dimension $130\lambda \times 60\lambda$) with static rough boundary (blue) and 12 switchable mirrors (red). Each mirror (length 10λ) is set independently to a tilt-angle of $+15°$ (state of $+1$) or $-15°$ (state of -1). Monochromatic light is injected from the input port (*Top*) and exits through the output port (*Right*), producing a 1D speckle pattern (containing ~70 speckle grains). (*B* and *C*) Expansion coefficient $\bar{c}(d)$ vs. expansion order d for output field (*B*) and intensity (*C*). With increasing reflectivity ρ of the cavity boundary, the distribution of $\bar{c}(d)$ moves to higher order d. (*D*) Mean expansion order for output field $\bar{d}_E$ and intensity $\bar{d}$ grows with ρ. Since intensity is the square of field amplitude, it is slightly higher. (*E*) $\bar{d}$ scales almost linearly with the mean number of bounces of optical rays off the mirror-array $\bar{\nu}$. Solid markers are numerical data for different boundary reflectivity ρ. Green dashed line is a linear fit.

an increase of the variance of $\log[P(\zeta)]$ with $\bar{d}$, confirming the fluctuation of total output intensity with mirror configurations is enhanced by high-order nonlinear mapping. We note that anomalously localized states in diffusive random media can enhance intensity fluctuations (43), but they are absent in our scattering cavity, as confirmed by spatially uniform intensity distribution throughout the cavity (Fig. 3*A*).

In addition to the wave simulation results shown above, we experimentally measure the intensity statistics of output speckle patterns from the integrating sphere. To increase the order of nonlinear mapping, we divide the DMD into 10×10 macropixels and record the output speckle patterns for a large ensemble (>10,000) of random binary configurations of DMD macropixels. Fig. 5*A* shows the local intensity PDF, $P(\eta)$, is much more extended than that for 3×3 macropixels. Its heavy tail reflects stronger local intensity fluctuations for 10×10 macropixels. The extraordinary intensity values facilitate light focusing, i.e., enhancing local intensity of output light by optimizing the DMD configuration. Fig. 5*B* shows the fluctuation of total output intensity $P(\zeta)$. For 3×3 macropixels, $P(\zeta)$ has a narrow, symmetric distribution around $\zeta = 1$. It becomes much wider and skewed with a long tail for 10×10 macropixels. The broadening of $P(\zeta)$ increases the range of control of the total output intensity (transmittance) by manipulating the scattering potential with the DMD.

The high-order nonlinear mapping also enhances spatial correlations of intensity fluctuations with scattering potentials. In Fig. 5*C*, the spatial correlation of $\eta(r)$, described by $C(\Delta r) \equiv \langle \eta_k(r)\, \eta_k(r+\Delta r)\rangle_{r,k} - 1$, is compared to that of $\tilde{\eta}(r)$ by $\tilde{C}(\Delta r) \equiv \langle \tilde{\eta}_k(r)\, \tilde{\eta}_k(r+\Delta r)\rangle_{r,k} - 1$. $C(\Delta r)$ exceeds $\tilde{C}(\Delta r)$. Their difference $\Delta C(\Delta r) \equiv C(\Delta r) - \tilde{C}(\Delta r)$ decays slower with Δr than $\tilde{C}(\Delta r)$, revealing the increased range of correlation. In contrast, $C(\Delta r)$ is almost equal to $\tilde{C}(\Delta r)$ for 3×3 macropixels

Downloaded from https://www.pnas.org by YALE UNIVERSITY CTR FOR SCI & SOCIAL SCI INFO on July 31, 2023 from IP address 130.132.173.101.

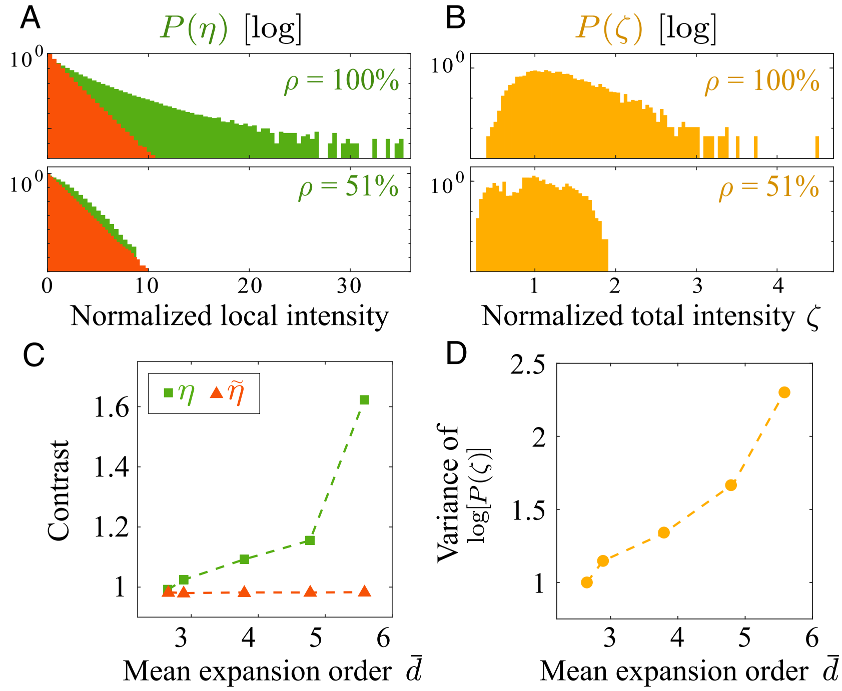

Fig. 4. Output intensity fluctuations. (*A*) PDF $P(\eta)$ of local intensity (normalized by the mean of all mirror configurations) η. With increasing boundary reflectivity ρ, $P(\eta)$ becomes broader and develops a tail (Green). PDF $P(\tilde{\eta})$ of intensity normalized by the spatial-average for individual mirror configuration (Red) exhibits an exponential decay, regardless of ρ. (*B*) PDF of the total output intensity for individual mirror configuration, $P(\zeta)$, is widened and skewed with increasing ρ. Fluctuations of local and total output intensities are stronger with higher-order nonlinear mapping. (*C*) Contrast of η increases with the effective order of nonlinear mapping $\bar{d}$, while contrast of $\tilde{\eta}$ remains close to 1. (*D*) Variance of $\log[P(\zeta)]$ grows with $\bar{d}$. All the results are obtained from wave simulation of a 2D cavity with parameters identical to those in Fig. 3.

(not shown). This confirms that the enhanced correlation of intensity fluctuations results from high-order nonlinear mapping.

4. Discussion and Conclusion

The multiple-scattering-induced nonlinear mapping discussed in this work does not rely on applied high-power electromagnetic field. This independence of high optical power is in stark contrast to conventional nonlinear optics based on intrinsic material response. While nonlinear optical materials can generate new frequencies of light, the frequency of output light from the multiple-scattering cavity is identical to the input one. Only the relation between output fields and reconfigured scattering potential (DMD configuration) is nonlinear due to multiple scattering by the potential.

Our method of achieving highly nonlinear mapping is robust, flexible, and power efficient. Such tunable nonlinearity will have a variety of applications, for example, the enhancement the security of optical scattering PUFs by introducing complex nonlinear mapping between challenge and response (44). An-

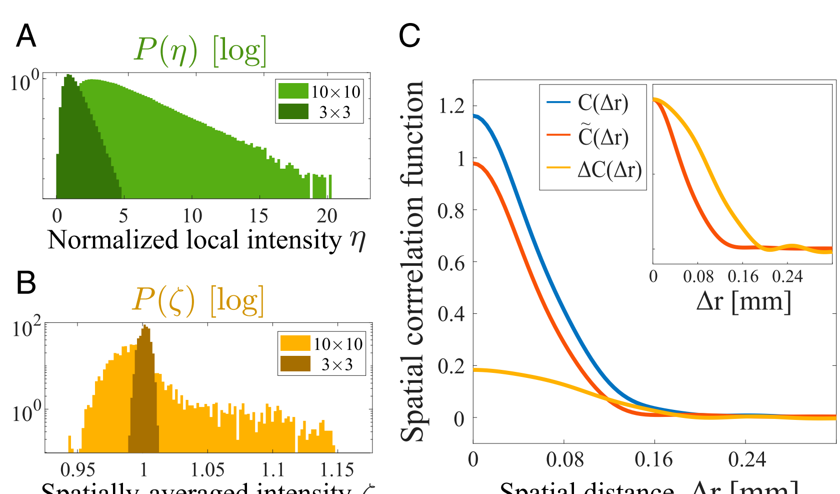

Fig. 5. Measured speckle statistics. (*A* and *B*) Probability density function of local speckle intensity η in (*A*) and of total output intensity ζ in (*B*) is much broader with a heavy tail for 10 × 10 macropixels than that for 3 × 3 macropixels. (*C*) Spatial correlation $C(\Delta r)$ of η is stronger than that $\tilde{C}(\Delta r)$ of $\tilde{\eta}$. Their difference $\Delta C(\Delta r) = C(\Delta r) - \tilde{C}(\Delta r)$ (normalized by $\Delta C(0)$ in the inset) has a larger width than $\tilde{C}(\Delta r)$. Spatial correlation of local intensity fluctuation is enhanced with 10 × 10 macropixels.

Downloaded from https://www.pnas.org by YALE UNIVERSITY CTR FOR SCI & SOCIAL SCI INFO on July 31, 2023 from IP address 130.132.173.101.

other application would be optical implementation of deep neural networks (45) and large-scale reservoir computing (5). Current approaches mostly rely on linear light diffraction or scattering and external digital nonlinearity, because conventional optical nonlinearities are power consuming and difficult to integrate. Our platform combines linear mixing and nonlinear mapping at low power and can be integrated on-chip to realize programmable linear and nonlinear operations for neuromorphic computing. Another possible direction is the realization large-scale photonic Ising machines for parallel processing of a vast number of spins (46, 47). Furthermore, our quantitative analysis of nonlinear mapping can be adopted to assess wireless communication channels (33) and their dependence on the reconfigurable intelligent surfaces (RIS). This will facilitate the utilization of RIS to control signal reception in reverberate chambers. Therefore, we expect the current platform in particular and such high-order nonlinear mapping in general to have diverse applications in metrology, optical computing, communication, and cryptography.

Data, Materials, and Software Availability. The theoretical and numerical findings can be reproduced using the information presented in the paper or *SI Appendix*. The original measured data used in the experiments has been uploaded to Zenodo (https://doi.org/10.5281/zenodo.8126899) (48), and the ensuing results can be obtained by following what is presented in the paper.

ACKNOWLEDGMENTS. This work is supported by the US Air Force Office of Scientific Research under Grant No. FA9550-21-1-0039. We would like to thank Seng Fatt Liew, Brandon Redding, Hasan Yılmaz, KyungDuk Kim, SeungYun Han, Liam Shaughnessy, Chen Chun-Wei, Asaf Lotz, Rasmus Rasche, Michael Lachner, Adomas Baliuka, Sara Nocentini, Giuseppe Emanuele Lio and Francesco Riboli for valuable information and stimulating discussions. We acknowledge the computational resources provided by the Yale High Performance Computing Cluster (Yale HPC). S.B. acknowledges the support for the Chair in Photonics from Ministère de l'Enseignement Supérieur, de la Recherche et de l'Innovation; Région Grand-Est; Département Moselle; European Regional Development Fund; Metz Métropole; GDI Simulation; CentraleSupélec; Fondation CentraleSupélec.

Author affiliations: [a]Department of Applied Physics, Yale University, New Haven, CT 06520; [b]Electrical and Computer Engineering Department, University of Connecticut, Storrs, CT 06249; [c]Institute for Computer Science, Ludwig Maximilian University of Munich, 80538 München, Germany; [d]Security in Telecommunications, Department of Software Engineering and Theoretical Computer Science, Technische Universität Berlin, Berlin, Germany; [e]Chair in Photonics, CentraleSupélec, Optical Materials, Photonics and Systems Laboratory, Metz 57070, France; and [f]Université de Lorraine, Chair in Photonics, CentraleSupélec, Optical Materials, Photonics and Systems Laboratory, Metz 57070, France

1. H. Cao, Y. Eliezer, Harnessing disorder for photonic device applications. *Appl. Phys. Rev.* **9**, 011309 (2022).
2. F. Pavanello, I. O'Connor, U. Rührmair, A. C. Foster, D. Syvridis, "Recent advances in photonic physical unclonable functions" in *2021 IEEE European Test Symposium (ETS)* (IEEE, 2021), pp. 1–10.
3. S. Sunada, A. Uchida, Photonic reservoir computing based on nonlinear wave dynamics at microscale. *Sci. Rep.* **9**, 1–10 (2019).
4. G. Wetzstein *et al*., Inference in artificial intelligence with deep optics and photonics. *Nature* **588**, 39–47 (2020).
5. M. Rafayelyan, J. Dong, Y. Tan, F. Krzakala, S. Gigan, Large-scale optical reservoir computing for spatiotemporal chaotic systems prediction. *Phys. Rev. X* **10**, 041037 (2020).
6. S. Sunada, K. Kanno, A. Uchida, Using multidimensional speckle dynamics for high-speed, large-scale, parallel photonic computing. *Opt. Express* **28**, 30349–30361 (2020).
7. G. Marcucci, D. Pierangeli, C. Conti, Theory of neuromorphic computing by waves: Machine learning by rogue waves, dispersive shocks, and solitons. *Phys. Rev. Lett.* **125**, 093901 (2020).
8. M. Segev, Y. Silberberg, D. N. Christodoulides, Anderson localization of light. *Nat. Phot.* **7**, 197–204 (2013).
9. H. Frostig *et al*., Focusing light by wavefront shaping through disorder and nonlinearity. *Optica* **4**, 1073–1079 (2017).
10. V. E. Kravtsov, V. M. Agranovich, K. I. Grigorishin, Theory of second-harmonic generation in strongly scattering media. *Phys. Rev. B* **44**, 4931–4942 (1991).
11. I. Tiginyanu *et al*., Semiconductor sieves as nonlinear optical materials. *Appl. Phys. Lett.* **77**, 2415–2417 (2000).
12. V. Mel'nikov *et al*., Second-harmonic generation in strongly scattering porous gallium phosphide. *Appl. Phys. B* **79**, 225–228 (2004).
13. J. Trull *et al*., Second-harmonic parametric scattering in ferroelectric crystals with disordered nonlinear domain structures. *Opt. Express* **15**, 15868–15877 (2007).
14. S. Faez, P. M. Johnson, D. A. Mazurenko, A. Lagendijk, Experimental observation of second-harmonic generation and diffusion inside random media. *J. Opt. Soc. Am. B* **26**, 235–243 (2009).
15. C. Yao, F. J. Rodriguez, J. Martorell, Controlling the diffused nonlinear light generated in random materials. *Opt. Lett.* **37**, 1676–1678 (2012).
16. S. A. Gredeskul, Y. S. Kivshar, Propagation and scattering of nonlinear waves in disordered systems. *Phys. Rep.* **216**, 1–61 (1992).
17. S. E. Skipetrov, R. Maynard, Instabilities of waves in nonlinear disordered media. *Phys. Rev. Lett.* **85**, 736–739 (2000).
18. B. Spivak, A. Zyuzin, Mesoscopic sensitivity of speckles in disordered nonlinear media to changes of the scattering potential. *Phys. Rev. Lett.* **84**, 1970–1973 (2000).
19. U. Bortolozzo, S. Residori, P. Sebbah, Experimental observation of speckle instability in Kerr random media. *Phys. Rev. Lett.* **106**, 103903 (2011).
20. M. Born, Quantenmechanik der stoßvorgänge. *Z. Phys.* **38**, 803–827 (1926).
21. B. Freedman *et al*., Wave and defect dynamics in nonlinear photonic quasicrystals. *Nature* **440**, 1166–1169 (2006).
22. T. Schwartz, G. Bartal, S. Fishman, M. Segev, Transport and Anderson localization in disordered two-dimensional photonic lattices. *Nature* **446**, 52–55 (2007).
23. A. Fleming, C. Conti, A. Di Falco, Perturbation of transmission matrices in nonlinear random media. *Ann. Phys.* **531**, 1900091 (2019).
24. M. Leonetti, S. Karbasi, A. Mafi, C. Conti, Experimental observation of disorder induced self-focusing in optical fibers. *Appl. Phys. Lett.* **105**, 171102 (2014).
25. K. M. Douglass, S. Sukhov, A. Dogariu, Superdiffusion in optically controlled active media. *Nat. Photonics* **6**, 834–837 (2012).
26. S. Bianchi, R. Pruner, G. Vizsnyiczai, C. Maggi, R. Di Leonardo, Active dynamics of colloidal particles in time-varying laser speckle patterns. *Sci. Rep.* **6**, 1–7 (2016).
27. N. Kaina, M. Dupré, G. Lerosey, M. Fink, Shaping complex microwave fields in reverberating media with binary tunable metasurfaces. *Sci. Rep.* **4**, 1–8 (2014).
28. M. Dupré, P. del Hougne, M. Fink, F. Lemoult, G. Lerosey, Wave-field shaping in cavities: Waves trapped in a box with controllable boundaries. *Phys. Rev. Lett.* **115**, 017701 (2015).
29. P. Del Hougne *et al*., Dynamic metasurface aperture as smart around-the-corner motion detector. *Sci. Rep.* **8**, 1–10 (2018).
30. P. del Hougne, G. Lerosey, Leveraging chaos for wave-based analog computation: Demonstration with indoor wireless communication signals. *Phys. Rev. X* **8**, 041037 (2018).
31. P. Del Hougne, M. Fink, G. Lerosey, Optimally diverse communication channels in disordered environments with tuned randomness. *Nat. Elect.* **2**, 36–41 (2019).
32. J. B. Gros, G. Lerosey, F. Mortessagne, U. Kuhl, O. Legrand, Uncorrelated configurations and field uniformity in reverberation chambers stirred by reconfigurable metasurfaces. *Appl. Phys. Lett.* **118**, 144101 (2021).
33. A. Rabault *et al*., On the tacit linearity assumption in common cascaded models of ris-parametrized wireless channels. arXiv [Preprint] (2023). http://arxiv.org/abs/2302.04993 (Accessed 14 March 2023).
34. Mv. van Rossum, T. M. Nieuwenhuizen, Multiple scattering of classical waves: Microscopy, mesoscopy, and diffusion. *Rev. Mod. Phys.* **71**, 313 (1999).
35. S. Rotter, S. Gigan, Light fields in complex media: Mesoscopic scattering meets wave control. *Rev. Mod. Phys.* **89**, 015005 (2017).
36. S. Resisi, Y. Viernik, S. M. Popoff, Y. Bromberg, Wavefront shaping in multimode fibers by transmission matrix engineering. *APL Photonics* **5**, 036103 (2020).
37. J. Kahn, G. Kalai, N. Linial, *The Influence of Variables on Boolean Functions* (Citeseer, 1989).
38. N. Linial, Y. Mansour, N. Nisan, Constant depth circuits, Fourier transform, and learnability. *J. ACM (JACM)* **40**, 607–620 (1993).
39. R. O'Donnell, *Analysis of Boolean Functions* (Cambridge University Press, 2014).
40. N. Wisiol *et al*., *pypuf: Cryptanalysis of Physically Unclonable Functions* (Zenodo, 2021).
41. R. Höhmann, U. Kuhl, H. J. Stöckmann, L. Kaplan, E. J. Heller, Freak waves in the linear regime: A microwave study. *Phys. Rev. Lett.* **104**, 093901 (2010).
42. C. Liu *et al*., Triggering extreme events at the nanoscale in photonic seas. *Nat. Phys.* **11**, 358–363 (2015).
43. T. Kottos, Statistics of resonances and delay times in random media: Beyond random matrix theory. *J. Phys. A: Math. General* **38**, 10761 (2005).
44. R. Pappu, B. Recht, J. Taylor, N. Gershenfeld, Physical one-way functions. *Science* **297**, 2026–2030 (2002).
45. X. Lin *et al*., All-optical machine learning using diffractive deep neural networks. *Science* **361**, 1004–1008 (2018).
46. Y. Yamamoto *et al*., Coherent Ising machines–optical neural networks operating at the quantum limit. *npj Quant. Inf.* **3**, 49 (2017).
47. D. Pierangeli, G. Marcucci, C. Conti, Large-scale photonic Ising machine by spatial light modulation. *Phys. Rev. Lett.* **122**, 213902 (2019).
48. Y. Eliezer *et al*., Data from "Tunable nonlinear optical mapping in a multiple-scattering cavity". Zenodo. https://zenodo.org/record/8126899. Deposited on July 8, 2023.

Downloaded from https://www.pnas.org by YALE UNIVERSITY CTR FOR SCI & SOCIAL SCI INFO on July 31, 2023 from IP address 130.132.173.101.